

# PRECISION CONTROLLED ACTUATION AND VIBRATION ISOLATION UTILIZING MAGNETORHEOLOGICAL (MR) FLUID TECHNOLOGY

Shawn P Kelso, Project Engineer, Ross Blankinship, Associate Principal Engineer  
 CSA Engineering, Inc., 2021 Girard SE, Suite 112, Albuquerque, NM 87106  
 Benjamin Kyle Henderson, Research Aerospace Engineer, AFRL/VSSV

## ABSTRACT

Precision controlled vibration isolation utilizing magnetorheological (MR) fluid technology for potential space optical applications, such as surveillance and directed energy, is addressed. This research includes the design, development and preliminary testing of a semi-active, proof-of-concept, MR vibration isolator. Base disturbances designed to produce payload vibration responses were employed in a single degree-of-freedom test apparatus. The MR vibration isolator served as the load-coupling element between the payload and the base disturbance input. The three-parameter isolator consists of two passive spring elements combined with one MR damping element. The MR damper control algorithm uses relative rate between damper cylinder and piston to dynamically vary the effective coefficient of damping. The result of this technology is ability to tune isolation frequency within a given range. Through intelligent modulation of the damping element alone, dynamic changes in both apparent stiffness and damping of the isolator are achieved. For applications where the ability to vary stiffness and damping would improve pointing accuracy and jitter control, this technology holds great appeal.

## INTRODUCTION

For space optical systems, such as surveillance and directed energy systems, the benefits resulting from effective vibration isolation and mitigation are numerous. Local optical jitter environments have the potential to reduce outgoing beam quality or incoming image quality. Local vibration environments cause unwanted optic jitter. The vibration disturbances for these systems often vary through time, with respect to magnitude and spectral distribution of vibration energy, and can be event-driven. Methodologies for dealing with these vibration environments include active, passive, semi-active or hybrid vibration mitigation systems.

Active solutions utilize actuation to address the effects of vibration inputs on sensitive hardware. An active system generates energy correspondent to the nature of the disturbance. These systems are intelligent and fast acting: they sense the vibration environment and

quickly respond. However, because these systems put energy into the system, the risk of damage caused by system instability exists. Also, should power not be available for some reason, the system cannot provide isolation in a passive manner; by definition, these systems are not fail-safe.

Hybrid vibration isolation systems for such applications employ actuation in addition to passive isolation to aid in vibration mitigation. Like the active solution, these systems have the capability to intelligently respond to changing inputs. Another benefit is that the hybrid solution can provide some level of isolation in the absence of power. However, the same risk of instability present in the active solution exists.

Passive vibration isolation solutions for space optical systems hold great attraction for quelling base disturbance, as they do not require power to operate, and with the exception of mechanical failure, are always capable of mitigating vibration. The major disadvantage of these solutions is that they represent a compromise: they provide single, fixed values of energy storage and absorption regardless of the magnitude and nature of the disturbance supplied.

This same 'passive compromise' is also found in the majority of automobile suspension systems available today. Most automotive suspension systems are engineered to quell typical vibration for a range of vehicle payloads and road-noise inputs. However, when higher-energy disturbances such as potholes, washboard roads, debris on the roadway, and emergency braking occur, the capabilities of the suspension system are often exceeded. The result of such events affects the safe operation and ride quality of the vehicle, the disadvantage of the compromise.

When dealing with more precise optic jitter concerns, these passive vibration isolation systems often do not possess the performance range to adequately mitigate the all the types of vibration energy that can be introduced. The result is a system that is either too soft or too stiff. This can result in an increase of the structural requirements of local optic structures, supporting hardware, etc.

The semi-active solution for vibration isolation offers an attractive alternative to active, passive, or hybrid systems. The semi-active approach utilizes the benefits of the other types while reducing the risks associated with these options. The benefits of the semi-active approach for this research include:

- *Provide active response* – the isolation system can sense and actively respond to varying inputs
- *A true fail-safe solution* – In the absence of power, the system provides full passive isolation
- *Is purely dissipative* – the system cannot put energy into the structure it supports; the risk of damage caused by instability is non-existent

A semi-active solution with the aforementioned benefits possesses the capability to reduce vibration response in a similar manner as a full-active system without the inherent risks.

**DESCRIPTION OF RESEARCH**

This research was focused on investigating the performance of a three-parameter isolator that utilizes a magnetorheological (MR) damper as the semi-active element. The three-parameter isolator consisted of two passive springs, one of which is in series with the controllable damper (see Figure 1). It should be noted that series spring,  $K_2$ , is 35 times stiffer than parallel spring,  $K_1$ .

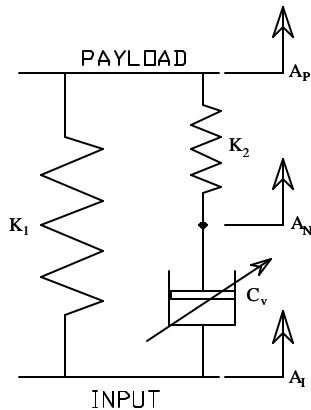


Figure 1 Field graphical representation of the three-parameter isolator model.

A feedback control algorithm was developed to actively vary the force required to extend or compress the damper, according to the nature of the input. Digital signal processing (DSP) code of the control algorithm was developed to modulate current of the DC power supply for the damper.

As mentioned, the controllable element of the isolator is the MR damper. The MR damper has the capability of delivering a broad range of damping force. Significant characterization testing of the damper was performed to generate look-up tables for the control algorithm’s use. Variable damping force results from varying electric current supplied to the damper. With no current supplied, the damper produces the base level of viscous damping.

A single degree-of-freedom, proof-of-concept isolator and payload support frame was fabricated for testing. Independent motion of the payload was constrained to single degree-of-freedom motion along the same axis of motion as the isolator as well as the base disturbance input supplied to the test setup.

**SEMI-ACTIVE CONTROL SYSTEM**

Recall from Figure 1 that the series spring,  $K_2$ , and MR damper are in series. The mission of the control system is to vary damping force to dynamically vary the contribution of this spring to overall isolation stiffness. From the perspective of the spectral domain, it appears that the stiffness of the isolator changes (see Figure 2).

In Figure 2, two transmittance plots are overlaid on the same graph to show the range of isolation control. The control algorithm effectively changes the *apparent stiffness\** of the isolator, resulting in an increase in isolation frequencies from approximately 1.0Hz to approximately 3.0Hz.

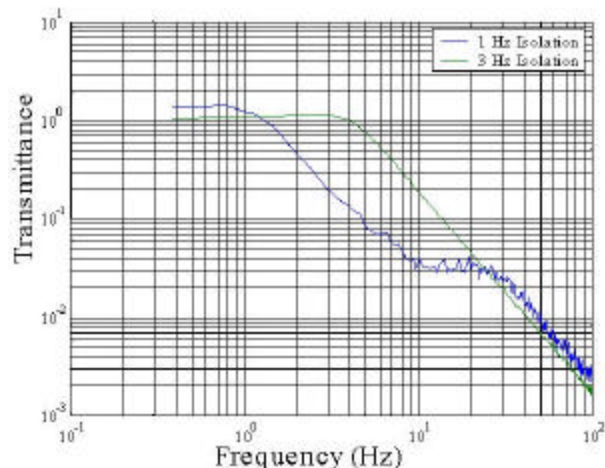


Figure 2 Simulated results of transmittance for the MR isolator.

\* *Apparent stiffness* refers to the fact that spring stiffness values have not changed; only the dynamic level of contribution of the series spring,  $K_2$ .

Damping rate estimation calculates the relative rate across the damper. Inputs to the DSP controller are accelerations at either end of the damper ( $A_N$  and  $A_I$ , for reference, see Figure 1). These accelerations are differenced, yielding relative acceleration, and then integrated, yielding relative rate.

The control scheme is a non-linear function of desired force and damper rate, and includes four coefficients that approximate MR damper behavior. They are:

1. Constant force (with sign opposite rate), representing Coulomb friction,
2. Force proportional to rate only, representing zero-field damping,
3. Force proportional to current only, and
4. Force proportional to the product of rate and current.

The commanded current output from this function is scaled into voltage. This commanded voltage is output from the DSP and converted into an analog signal, which then drives the power amplifier for the MR coil.

#### MAGNETORHEOLOGICAL (MR) DAMPER

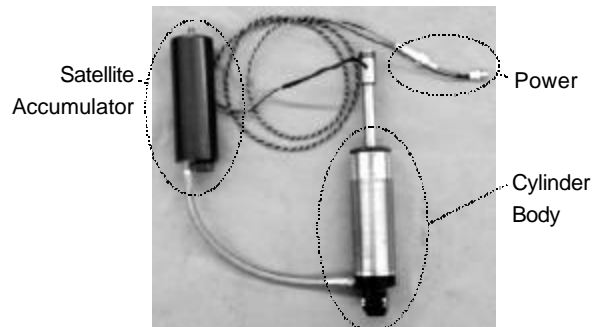


Figure 3 Photo of the engineering prototype MR damper

To facilitate testing and internal access, an engineering prototype damper was developed (see Figure 3). The damper contains Magnetorheological (MR) fluid. The viscous medium is comprised of a base fluid (silicon oil or ethanol glycol) that contains ferrous particles. These particles polarize when introduced to a magnetic field (see Figure 4). The polarization of the particles causes a magnetic attraction, which in turn results in the formation of chains and columns of particles. The presence of the chains and columns result in an increase of the apparent viscosity of the fluid. As the fluid moves through the field normal to the vector of the field lines, the change in viscosity translates to a change in damping force.

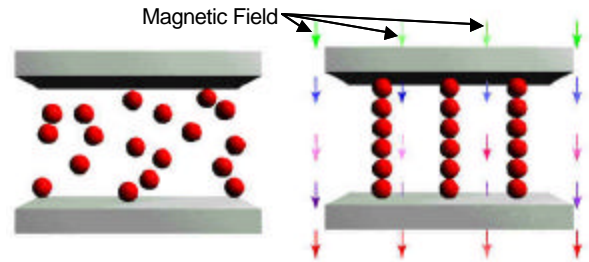


Figure 4 An illustration of MR fluid at rest (a), and within a magnetic field (b).

The magnetic field for this damper design is generated within the body of the damper piston. As the piston reciprocates within the damper cylinder, fluid traverses the orifices of the piston. Adjacent to these orifices, internal electromagnets generate variable levels of magnetic field, depending upon the level of electric current delivered by the power supply.

#### THE ELECTROMAGNETIC CIRCUIT OF THE MR DAMPER

One benefit of using MR fluid for varying damping force in lieu of a mechanical method is in device response time: the time required to change apparent viscosity of MR fluid is far less than the time a mechanical system requires to vary orifice size [6]. It is the design intent of this MR damper to accommodate feedback control strategies across a broad frequency spectrum. Oftentimes the damper is the limiting factor achieving the highest bandwidth of control, typically due to the device's time response. Typically, an MR fluid device's time response is limited to the time response of the electromagnetic circuit that creates the required flux density within the MR-gap. The design challenge exists in creating a DC electromagnetic circuit that can generate sufficient flux across the MR-gap in a minimum amount of time.

Time response for an electromagnetic circuit can be modeled as a function of inductance and electrical resistance. This can be expressed as:

$$t = \frac{L}{R} \quad (1)$$

Where  $t$  is time response,  $L$  is inductance, and  $R$  is resistance. Minimizing the  $L/R$  ratio reduces time constant of the electromagnetic circuit. However, generating sufficient flux in the MR-gap using a 'practical' amount of electrical current, under 6A maximum in this case, requires the existence of a minimum number of coil windings,  $N$  [8, 9]. This results in a value of electrical resistance correspondent to the total length of magnet wire required. Only one

remaining parameter can be manipulated in order to reduce the time response: the inductance. As represented in Figure 5, inductance of the coil,  $L_C$ , can be represented as [10]:

$$L_C = \frac{4p^2 N^2 r^2 K_n}{l} \cdot 10^{-6} \quad (2)$$

whose units are in Henries, with radius in terms of inches. The geometry term,  $K_n$ , in Equation (2) is defined as [10]:

$$K_n = \frac{1}{1 + 0.9\frac{r}{l} + 0.32\frac{t}{r} + 0.84\frac{t}{l}} \quad (3)$$

Where  $r$  is the mean radius,  $t$  is thickness, and  $l$  is length of the coil along the centerline. Decrease in inductance results from the manipulation of these area terms. Consider the two images presented in Figure 5 and Figure 6. Figure 6 shows an arrangement of three smaller coils whose sum cross-sectional area is equivalent to the area of the single coil shown in Figure 5. It is assumed that the same number of coils and type of magnet wire is used for both cases, hence equivalent values for electrical resistance. The inductance of the electromagnetic circuit in Figure 5 is calculated directly from Equation (2). Inductance for the series electromagnetic circuit of Figure 6 must account for the effects of mutual inductance in addition to the series addition of three individual coil inductances [5]:

$$L_S = L_1 + L_2 + L_3 \pm 2(M_{12} + M_{23} + M_{13}) \quad (4)$$

Where  $L_S$  is the summed inductance,  $L_1$  is inductance of the first coil,  $L_2$  the second, and  $L_3$  the third.  $M_{12}$  is mutual inductance for the interaction between the first and second coil,  $M_{23}$  is mutual inductance for the interaction between the second and third coils, and  $M_{13}$  is mutual inductance of the external two coils. The plus/minus sign before the mutual inductance terms indicates that coupling is either additive or subtractive, depending on the connection polarity.

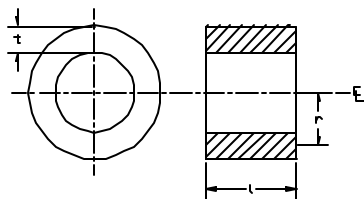


Figure 5 Cross-sectional view of solenoid coil

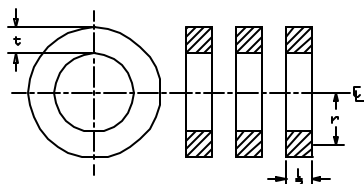


Figure 6 Cross-sectional views of 3 coils in series

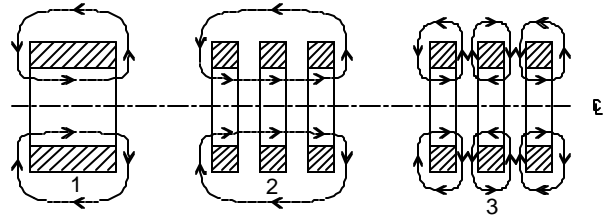


Figure 7 Flux paths for three different coil configurations. The direction of wind is constant in #1 & #2 and alternates in #3.

Figure 7 illustrates the difference in connection polarity. Coil configuration #1 has flux lines that flow around the single coil. Coil configurations #2 and #3 represent two three-coil arrangements with similar characteristics except for polarity. Configuration #2 illustrates the flow of flux around three coils with windings in the one direction relative to the centerline. Configuration #3 illustrates the flow of flux around three coils whose winding orientations alternate for each coil. The main difference between the two configurations is the length of the flux paths. The benefit of the coil arrangement on configuration #3 is that the overall inductance of the circuit is much lower than the previous two cases; the mutual inductances are subtracted from overall inductance, hence:

$$L_{\#3} \ll L_{\#1} \quad \& \quad L_{\#3} \ll L_{\#2} \quad (5)$$

The result is a comparatively shorter time response with configuration #3 than with configurations #1 or #2. One issue of concern with generating smaller local flux paths such as those found in configuration #3 is the usefulness of the flow of magnetic flux in terms of generating the desired MR-effect. The MR-gap of the MR damper used in this research takes this arrangement into account and delivers the required performance in addition to the benefit of the reduced time response.

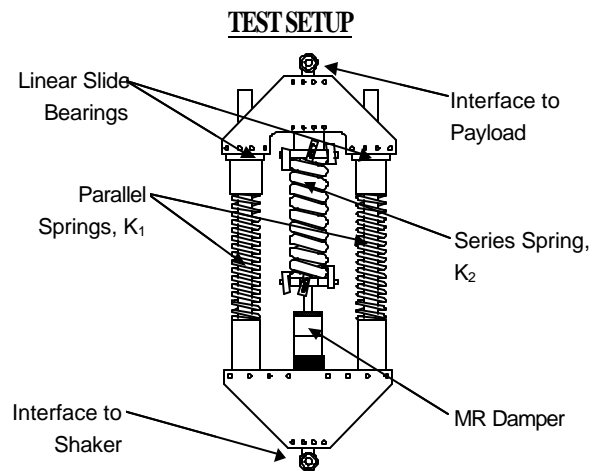


Figure 8 Illustration of the proof-of-concept test isolator

The MR damper was integrated as the semi-active element of the 3-parameter isolator. Figure 8 is a drawing of the isolator as it was tested in the payload frame. The linear bearings of the isolator constrain motion to a single degree-of-freedom. The two outboard springs serve as the parallel spring,  $K_1$ . The large spring in series with the damper,  $K_2$ , is there to provide the steeper roll-off associated with three-parameter damping. The isolator uses a coil-capturing mechanism that grabs only the first and last coils of the spring, so as not to change spring rate. Ball-end joints at the top and bottom of the isolator serve as mounting points and ensure that only axial loading of the isolator occurs.

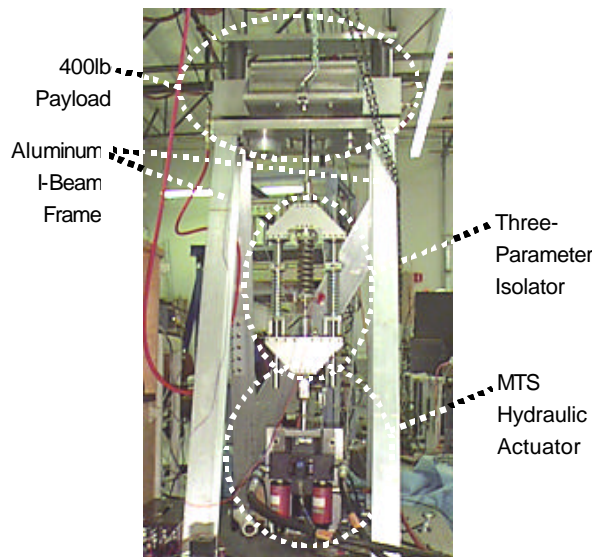


Figure 9 Photograph of the single degree-of-freedom isolator in the load frame.

Figure 9 is a photograph of the isolator mounted in the load frame. The isolator and payload were scaled for this test frame. A tray for the payload mass floats on air bearings (Figure 10) and constrains payload motion to single degree-of-freedom motion with very little local payload friction.

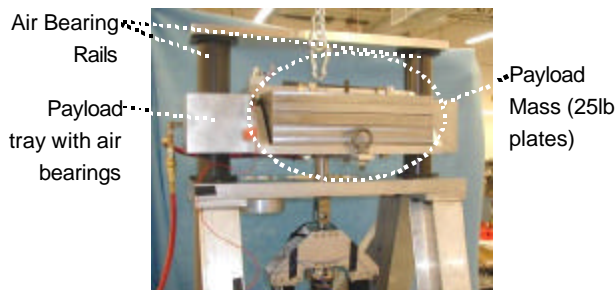


Figure 10 Close-up of the payload floating on air-bearings.

An hydraulic actuator at the bottom side of the isolator provided base motion input (Figure 10). Accelerometers were located on the payload, the bottom of the isolator, and at the node location between the series spring and MR damper. The signals of the base and the node between the damper and series spring were split and sent to the data acquisition system and the DSP controller. The three accelerometers were recorded with a WCA data acquisition system. The acceleration signals of the node and base were match-calibrated. These two analog accelerations were passed to the DSP controlling hardware, where they were digitized, differenced and integrated to become a relative rate signal, the input to the control algorithm.

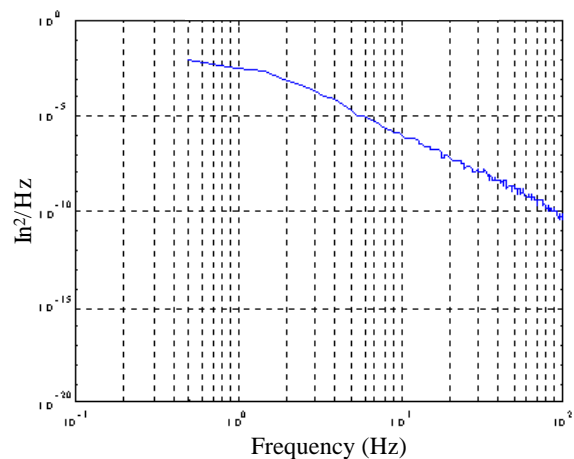


Figure 11 Typical base displacement power spectral density PSD plot of base disturbance

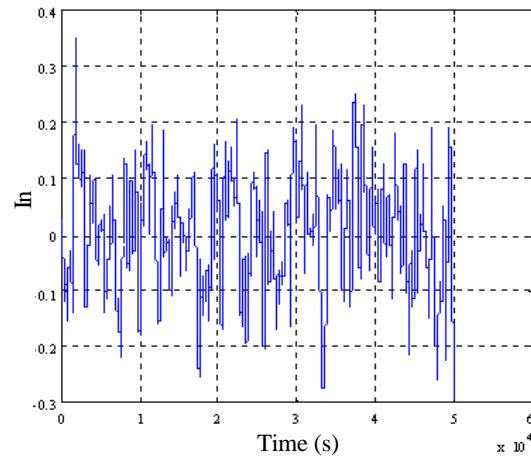


Figure 12 Typical time history plot of shaker input

Figure 11 is representative power spectral density (PSD) plot of the input used to drive the shaker. Figure 12 is a sample time history plot of the same disturbance. This signal was generated on a Wavetek Model 132 signal generator. The random excitation

function was chosen and an analog, second-order Butterworth filter circuit was added to the output signal of the Wavetek. The addition of the circuit filtered the magnitude of the output signal so that it produced the required corner frequency and decay slope (typical of anticipated SBL inputs). The hydraulic actuator was driven in displacement mode with this signal, providing the base disturbance. The magnitude of the signal was modulated by varying the gain on the signal generator.

**RESULTS**

DAMPING RANGE TESTING-LOW FREQUENCY

BEHAVIOR

The MR damper was first characterized independently of the complete isolator. The device was placed in a test fixture in between a load cell (attached to a rigid backing) and the hydraulic actuator. Several values of fixed amplitude and fixed frequency sine wave inputs were applied to the actuator. Force, velocity, and displacement were simultaneously recorded. This data provided the performance of the damper at frequency ranges between 0.5Hz and 4.0Hz.

Figure 13 are overlaid force versus velocity plots that illustrates the representative range of damping available with the MR damper. These results typify damping behavior throughout the frequency range of interest. The two plot lines in Figure 14 represent the range of damping for the minimum and maximum piston velocities tested. There is an associated peak damper piston velocity for each unique amplitude and frequency tested. The test range was from 0.5Hz, 0.125" peak to 4.0Hz, 0.5" peak, corresponding to velocities of 0.13in/s and 12.6in/s, respectively. The data in Figure 14 summarizes damper performance throughout the frequency range.

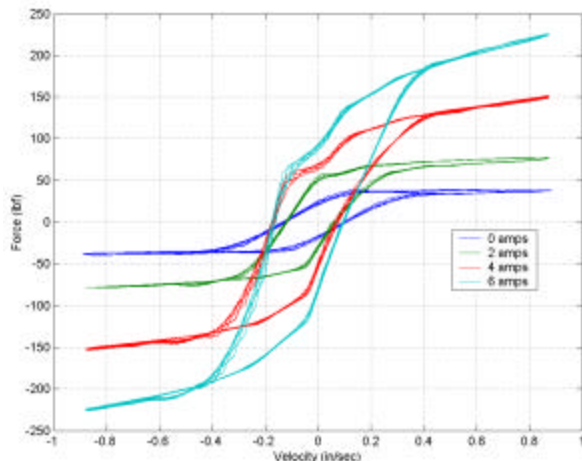


Figure 13 Typical force versus velocity for the MR damper at various supplied DC currents (2.0Hz test data)

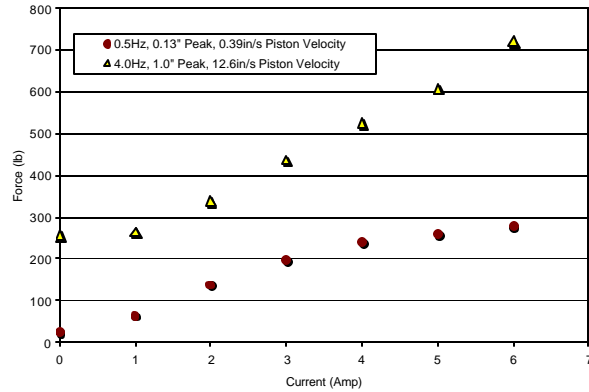


Figure 14 Force as a function of current for the range of velocities tested (0.5Hz, 0.125" peak to 4.0Hz, 1.0" peak)

DYNAMIC DAMPING COEFFICIENT-HIGH FREQUENCY

BEHAVIOR

Dynamic Complex Stiffness (DCS) testing is a test method that is used to determine the effective stiffness and damping of an isolator. One benefit of this type of testing is that it provides data on performance for a wide range of frequencies, unlike the envelope of frequencies and amplitudes presented in the previous section. In one test, a broad range of performance is investigated. With this testing, a random noise signal is introduced to the hydraulic actuator whose RMS voltage is a result of the percent gain set on the signal generator.

With typical DCS testing, displacement and force are measured. The former divided by the latter provides the value for stiffness. Phase is also captured because it is an indicator of the level of damping (the complex component) present.

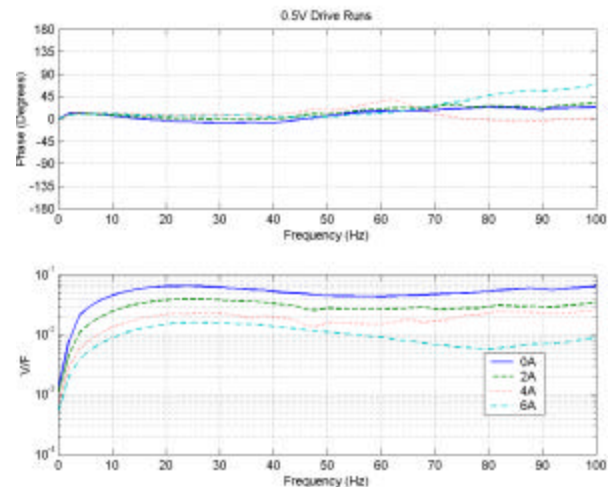


Figure 15 The inverse of damping ( $C^{-1}$ , velocity/force) and phase as a function of frequency for 0.5V RMS random excitation

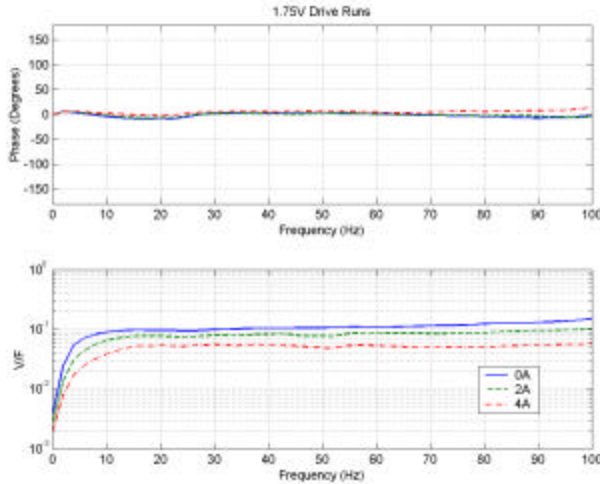


Figure 16 The inverse of damping ( $C^{-1}$ , velocity/force) and phase as a function of frequency for 1.75V RMS random excitation

Since this testing was performed on a damper, velocity was used as the numerator, providing the inverse of the coefficient of damping,  $C^{-1}$ .

Figure 15 and Figure 16 are DCS plots of the MR damper for random excitation inputs of 0.5V and 1.75V, the minimum and maximum values tested. The near constant phase at  $0^\circ$  shows that there is no spring component present. The linearity of the V/F ratio of the MR damper shows it is not dependent upon frequency. This consistent behavior is attractive for the application of feedback control because performance can be predicted accurately within the frequency bandwidth of interest. The roll-off found at frequencies below 10Hz are the result of insufficient input energy at those lower frequencies.

INITIAL THREE-PARAMETER ISOLATOR TESTS

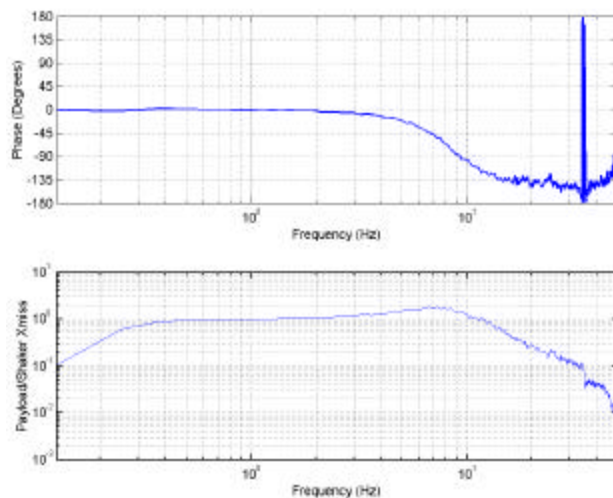


Figure 17 Passive behavior of the isolator

Initial isolator testing was performed in open loop, passive mode, with no current supplied to the damper. The reason for this testing was to generate the passive transmissibility function of the isolator. The performance of the isolator in this mode of operation represents the ‘fail-safe’ behavior of the isolator. As mentioned in the previous section, the hydraulic actuator excited the isolator and payload with the filtered random signal. Frequency response functions between input and payload were taken. The results of this testing is shown in Figure 17.

It should be noted that, at the time of the writing of this document, close-loop testing had yet to be completed. Future work includes further testing to generate performance data illustrating the shift in peak isolation frequency.

SUMMARY

This research has shown that the MR technology demonstrated produces a range of damping coefficients necessary for the modulation of the *apparent stiffness* of the three-parameter isolator. The potential exists for this technology to aid in line of sight (LOS) jitter reduction for directed energy and optic sensing space-borne systems.

A major benefit of this technology is that it provides a fail-safe to passive vibration isolation system. In the absence of power, sensing and semi-active control, passive, viscous damping still exists. Another benefit of this technology is the fact that it is purely dissipative. The risks associated with instability of the active element are non-existent

ACKNOWLEDGEMENTS

A portion of the work completed and currently underway was funded by a SBIR Phase 1 contract awarded by the Ballistic Missile Defense Organization, Dr. Benjamin Henderson, technical monitor. The author would like to acknowledge the support and mentoring provided by Mr. Jim Goodding of CSA Engineering. The author would also like to Acknowledge CSA Engineering’s Internal Research and Development program for providing funding for hardware development and testing.

REFERENCES

1. Kelso, S.P. “Experimental Characterization of Commercially Practical Magnetorheological Fluid Damper Technology,” *Proceedings of SPIE Conference on Smart Structures and Materials*,

- Paper No. 4332-34*, Newport Beach, CA, March, 2001.
2. F. Gordaninejad and S.P. Kelso, "Magneto-rheological fluid shock absorbers for HMMWV," *Proceedings of SPIE Conference on Smart Structures and Materials*, Paper No. 3989-21, Newport Beach, CA, March, 2000.
  3. Lord Materials Division, "Designing with MR Fluids", *Engineering Note*, Lord Corporation, Thomas Lord Research Center, Cary, NC, November 1999.
  4. Kelso, S. P. and Gordaninejad, F., "Magneto-Rheological Fluid Shock Absorbers for Off-Highway, High-Payload Vehicles," *Passive Damping and Isolation, Proceedings of the 1998 SPIE Conference on Smart Materials and Structures*, Ed. by L. Porter Davis Vol. 3672 pp. 44-54, 1999.
  5. T.A. Bowland, *Electrical Circuit Formulae*, p.5 BOWest Pty Ltd, 1998.
  6. M.R. Jolly, J.D. Carlson and J.W. Bender, "Properties and applications of commercial rheological fluids," *SPIE 5<sup>th</sup> Annual International Symposium on Smart Materials and Structures*, San Diego, CA, 15 March, 1998.
  7. F. Yeaple, *Fluid Power Design Handbook*, Third Edition, p. 683, Marcel Dekker, Inc., New York, 1996.
  8. Carlson, J. D., Catanzarite, D. M. and St. Clair, K. A., "Commercial Magneto-Rheological Fluid Devices," *Proceedings of the 5th International Conference on ER Fluids, MR Fluids and Associated Technology*, U. Sheffield, UK, pp. 20-28, 1995.
  9. M. A. Plonus, *Applied Electromagnetics*, p.221 McGraw Hill Book Company, New York, 1978.
  10. J. A. Wagner, "The Shorted Turn in the Linear Actuator of a High Performance Disk Drive", *Transactions on Magnetism*, Sperry Univac, Santa Clara, California, and San Jose State University, San Jose, CA, March 29, 1982.
  11. V.G. Wellsby, *The Theory and Design of Inductance Coils*, p.27 & 165, Macdonald & Co., (Publishers) Ltd., circa 1952